


ORIGINAL ARTICLE

First-principles study, fabrication, and characterization of (Hf_{0.2}Zr_{0.2}Ta_{0.2}Nb_{0.2}Ti_{0.2})C high-entropy ceramicBeilin Ye¹ | Tongqi Wen^{2,3} | Kehan Huang¹ | Cai-Zhuang Wang^{3,4} | Yanhui Chu¹ ¹School of Materials Science and Engineering, South China University of Technology, Guangzhou, China²MOE Key Laboratory of Materials Physics and Chemistry under Extraordinary Conditions, School of Natural and Applied Sciences, Northwestern Polytechnical University, Xi'an, China³Ames Laboratory-USDOE, Iowa State University, Ames, Iowa⁴Department of Physics and Astronomy, Iowa State University, Ames, Iowa

Correspondence

Yanhui Chu, School of Materials Science and Engineering, South China University of Technology, Guangzhou, China.
Email: chuyh@scut.edu.cn

Funding information

National Natural Science Foundation of China, Grant/Award Number: 51802100; National Key Research and Development Program of China, Grant/Award Number: 2017YFB0703200; CAST, Grant/Award Number: 2017QNRC001; U.S. Department of Energy; Iowa State University, Grant/Award Number: DE-AC02-07CH11358; National Energy Research Scientific Computing Center

Abstract

The formation possibility of (Hf_{0.2}Zr_{0.2}Ta_{0.2}Nb_{0.2}Ti_{0.2})C high-entropy ceramic (HHC-1) was first analyzed by the first-principles calculations, and then, it was successfully fabricated by hot-pressing sintering technique at 2073 K under a pressure of 30 MPa. The first-principles calculation results showed that the mixing enthalpy and mixing entropy of HHC-1 were -0.869 ± 0.290 kJ/mol and 0.805R, respectively. The experimental results showed that the as-prepared HHC-1 not only had an interesting single rock-salt crystal structure of metal carbides but also possessed high compositional uniformity from nanoscale to microscale. By taking advantage of these unique features, it exhibited extremely high nanohardness of 40.6 ± 0.6 GPa and elastic modulus in the range from 514 ± 10 to 522 ± 10 GPa and relatively high electrical resistivity of 91 ± 1.3 $\mu\Omega\cdot\text{cm}$, which could be due to the presence of solid solution effects.

KEYWORDS

electrical resistivity, first-principles calculations, high-entropy ceramics, mechanical properties, metal carbides

1 | INTRODUCTION

Crystalline high-entropy ceramics (CHCs), a new class of solid solutions that contain five or more elemental species, are attracting increasing interest for their unique structure and properties and potential applications.^{1,2} Generally, in CHCs, a maximum molar configurational entropy can be produced by mixing five or more elements in equimolar concentrations, which results in the minimization of Gibbs

free energy.^{3,4} As a result, these new materials can be thermodynamically more stable at elevated temperatures. More interestingly, much more unique physical and chemical characteristics that cannot be easily predicted from the crystal structure and the nature of the constituting elements can be achieved in CHCs due to their four core effects including high-entropy, lattice distortion, sluggish diffusion, and cocktail effect.^{5,6} Therefore, recent research highlighted the fabrication and properties of various CHCs, such as metal oxides,^{7,8} diborides,^{9,10} nitrides,¹¹ and carbides.^{12,13} Among the existing CHCs, metal carbide CHCs have

Beilin Ye and Tongqi Wen contributed equally to this work.

received great attention for potential applications in the structural fields, especially extreme conditions of temperature, pressure, and other, owing to their excellent physical and chemical properties including high hardness, melting point, good thermal stability, and corrosion resistance.^{14,15} Recently, Yan et al¹² prepared $(\text{Hf}_{0.2}\text{Zr}_{0.2}\text{Ta}_{0.2}\text{Nb}_{0.2}\text{Ti}_{0.2})\text{C}$ high-entropy monolithic ceramic with low thermal conductivity by spark plasma sintering technique at 2273 K under a pressure of 30 MPa. Zhou et al¹³ synthesized $(\text{Hf}_{0.2}\text{Zr}_{0.2}\text{Ta}_{0.2}\text{Nb}_{0.2}\text{Ti}_{0.2})\text{C}$ high-entropy ceramic powder by heat-treatment technique at 2223 K under vacuum. However, the current study and understanding of metal carbide CHCs are still limited.

In this work, we first analyzed the formation possibility of $(\text{Hf}_{0.2}\text{Zr}_{0.2}\text{Ta}_{0.2}\text{Nb}_{0.2}\text{Ti}_{0.2})\text{C}$ high-entropy ceramic (HHC-1) by the first-principles calculations and then successfully fabricated it by hot-pressing (HP) sintering technique at 2073 K under a pressure of 30 MPa. The phase evolution and crystal structure of the as-prepared HHC-1 were investigated, as well as their compositional uniformity, electrical resistivity, and mechanical properties.

2 | EXPERIMENTAL AND COMPUTATIONAL METHOD

The first-principles calculations based on the density functional theory (DFT) were carried out using Vienna Ab-Initio Simulation Package (VASP).^{16,17} The projected-augmented-waves (PAW) with the Perdew-Burke-Ernzerhof (PBE) exchange-correlation potentials were adopted.^{18,19} Generally, the binary metal carbides, including ZrC, HfC, TaC, NbC, and TiC, consist of two sets of face-centered cubic (FCC) sublattice. Consequently, a cell of the multi-component metal carbides was built, in which one FCC sublattice is occupied by C atoms and the other FCC sublattice is occupied by five kinds of metal atoms, as shown in Figure 1A. It is noted that this is a simplified schematic diagram that does not take the lattice distortion into account. In order to build a model closer in the stoichiometry of HHC-1 and investigate the mobility of each type of atoms, a $2 \times 2 \times 2$ supercell was built with 64 atoms in total, as displayed in Figure 1B. The first-principles calculations based on DFT focused on the supercell structure of HHC-1. To achieve decent statistics, the energies of 100 structures with random distribution of metal atoms and the stoichiometry nearly the same as HHC-1 were calculated. The energy and lattice constant of each binary metal carbide system were also calculated from a $2 \times 2 \times 2$ supercell. The energy calculations were performed using PAW method within VASP. Generalized gradient approximation in the form of PBE was used for the electronic exchange and correlation energy. The plane-wave cut-off energy of

400 eV was applied and the calculations were performed with the automatic k-mesh generation 40 in VASP. The electronic energy convergence criterion and the ionic force convergence criterion were 10^{-4} eV and 0.02 eV/Å, respectively. Furthermore, the positions of the atoms were allowed to relax during the calculation and the volume of the supercell was carefully adjusted to give a pressure less than 0.0 ± 1.0 kBar after relaxation. These selected calculation parameters were mainly based on Refs. [20–23].

HHC-1 was prepared by HP sintering technique in the furnace. The powders of ZrC, HfC, TaC, NbC, and TiC (99.9% purity, average particle size $<3 \mu\text{m}$, Shanghai ChaoWei Nanotechnology Co. Ltd., Shanghai, China) were utilized as starting materials. The powders were mixed as follows: 20 mol.% ZrC, 20 mol.% HfC, 20 mol.% TaC, 20 mol.% NbC, and 20 mol.% TiC, and ball-milled for 24 hours in ethanol using high-purity agate spherical media. Afterward, the powders were dried, screened, and pressed into pellets of 20 mm (diameter) \times 10 mm

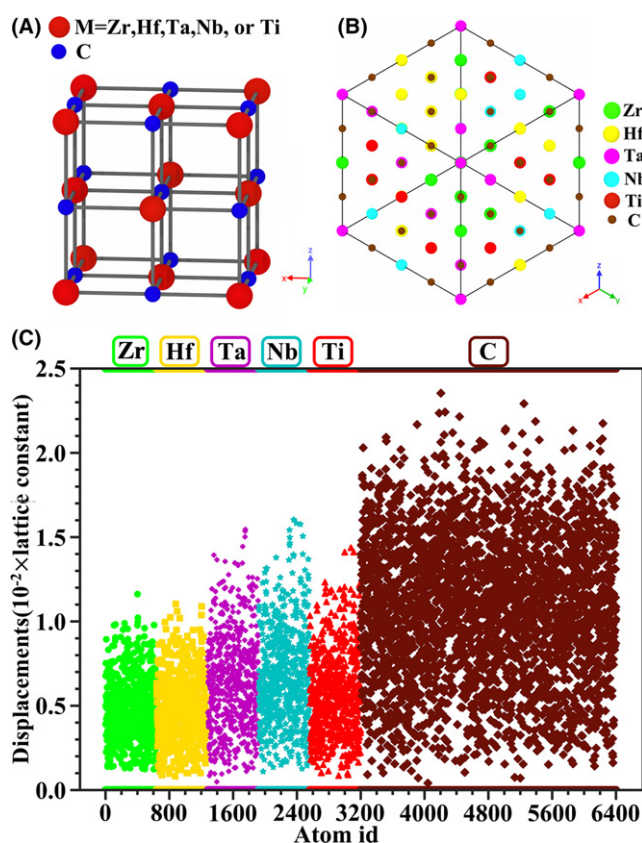


FIGURE 1 First-principles calculations analysis of HHC-1: (A) the simplified schematic diagram of unit cell that does not take the lattice distortion into account; (B) the structure model of the $2 \times 2 \times 2$ supercell with 64 atoms viewed from the [111] direction and the color of the atoms is the same as that in (A); (C) the atomic displacements of the different elements resulting from the relaxation expressed as the fraction of the lattice constant [Color figure can be viewed at wileyonlinelibrary.com]

(thickness) under a uniaxial pressure of 10 MPa. Finally, these pellets were hot-pressed under a mechanical pressure of 30 MPa inside graphite dies in vacuum at 2073 K for 30 minutes with a heating rate of 8 K/minute.

Phase analysis of the samples was monitored by X-ray diffraction (XRD, X'pert PRO, Almelo, the Netherlands). The equivalent counting time for a conventional point detector would be 30 seconds per point at $0.01^\circ 2\theta$ increments. The microstructure and compositional uniformity of the samples were analyzed by scanning electron microscopy (SEM, supra-55; Zeiss, Oberkochen, Germany) with energy dispersive spectroscopy (EDS) and transmission electron microscopy (TEM, JEM 2100, JEOL, Tokyo, Japan) with EDS. Nanoindentation test was performed on the well-polished surface of the samples using the Nano-IndenterTM XP (MTS system Corp., Minnesota, USA) system with a diamond Berkovich indenter with a tip radius of 20 nm to measure their nanohardness and elastic modulus. The load was set at a constant value (8 mN). The indentations were recorded with each point spaced 10 μm apart. The nanohardness and elastic modulus of the samples were calculated by the Oliver and Pharr method.²⁴ It should be mentioned that the elastic modulus is determined using the following equation:

$$1/E_{\text{eff}} = (1 - \nu^2)/E + (1 - \nu_I^2)/E_I \quad (1)$$

where E_{eff} is the reduced modulus obtained from nanoindentation, E and ν are the elastic modulus and Poisson's ratio, respectively, for the sample, whereas E_I and ν_I are the same parameters for the indenter. An estimated Poisson's ratio (0.18–0.22) from the average value of five individual metal carbides is obtained from literature²⁵ where available. The microhardness of the samples was measured on their well-polished surface by the indentation technique using the microhardness tester with a Vickers indenter (HVS-30Z, Shanghai SCTMC Co. Ltd., Shanghai, China) at different loads (0.98, 1.96, 2.94, 4.9, and 9.8 N). The fracture toughness of the samples was also measured on their well-polished surface by the indentation technique using the same microhardness tester with a Vickers indenter. A load of 24.5 N was used to generate the cracks in the sample in order to calculate the fracture toughness (K_{Ic}) by using the Antis equation:²⁶

$$K_{\text{Ic}} = 0.016 \left(\frac{E}{H} \right)^{1/2} \frac{P}{c^{3/2}} \quad (2)$$

where P is the applied load, E is the elastic modulus, H is the hardness, and c is the radial crack length (measured

from center of indent). A total of 30 indentations were performed to get the average value of the hardness, elastic modulus and fracture toughness. The electrical resistivity of HHC-1 at room temperature was determined by the four-point probe method with three specimens $1 \times 3 \times 10$ mm in size to get the average value. These experiments were carried out by using a digital DC resistance tester (TH2512, Tonghui Electronic Co. Ltd., Changzhou, China). The densities of the samples were measured via the Archimedes method and the relative densities were calculated via using theoretical densities that were determined by the lattice parameters measured by XRD.

3 | RESULTS AND DISCUSSION

The equilibrium lattice parameters of HHC-1 and the binary carbides at 0 K calculated by the first principles are listed in Table 1. It can be seen that the calculated lattice parameter of HHC-1 is about 4.528 ± 0.005 Å, in good agreement with the calculated lattice parameter of 4.524 Å from Vegard's law,²⁷ which demonstrates the calculated lattice constant of HHC-1 is reasonably accurate. Furthermore, on the basis of the energies from DFT calculations of HHC-1 and the binary carbides at 0 K after relaxation (Table 1), we can analyze whether or not the structure of HHC-1 is thermodynamically stable. The thermodynamic stability of HHC-1 is determined by its mixing Gibbs free energy (ΔG_{mix}), which can be expressed as:

$$\Delta G_{\text{mix}} = \Delta H_{\text{mix}} - T\Delta S_{\text{mix}} \quad (3)$$

where ΔH_{mix} is the mixing enthalpy of HHC-1, ΔS_{mix} is the mixing entropy of HHC-1, and T is the temperature. The ΔH_{mix} should be insensitive to the temperature thus its variation can be negligible.²⁸ As a consequence, the ΔH_{mix} of HHC-1 can be estimated by its value at 0 K. Specifically, the mixing enthalpy of HHC-1 at 0 K ($\Delta H_{\text{mix}}^{0\text{K}}$) can be calculated by the following equation:

$$\Delta H_{\text{mix}}^{0\text{K}} = E_{\text{HHC-1}} - (E_{\text{ZrC}} + E_{\text{HfC}} + E_{\text{TaC}} + E_{\text{NbC}} + E_{\text{TiC}})/5 \quad (4)$$

where E stands for the DFT energies of the different samples after relaxation at 0 K and 0 Pa. Using the energies

TABLE 1 Calculated equilibrium lattice parameters and DFT energies of the different samples at 0 K

Samples	HHC-1	ZrC	HfC	TaC	NbC	TiC
Lattice parameters (Å)	4.528 ± 0.005	4.704	4.641	4.474	4.477	4.324
Energies (eV/atom)	-10.207 ± 0.0253	-9.735	-10.526	-11.102	-10.277	-9.351

from DFT calculations, the $\Delta H_{\text{mix}}^{H0K}$ is calculated to be about -0.869 ± 0.290 kJ/mol, which is close to zero. According to the phase formation theory in multicomponent systems, the positive ΔH_{mix} and negative ΔH_{mix} have the same effect for restraining the solid solution formation. Only when the value of ΔH_{mix} is close to zero, the different elements can randomly distribute in the system, and the solid solution phases can stable occur in the solid phase.²⁹ In general, the mixing entropy of a system containing two different sublattices (h presents one sublattice with a number of sites X , and k presents another sublattice with a number of sites Y) can be defined as:^{30,31}

$$\Delta S_{\text{mix}} = -R \left\{ \frac{X}{X+Y} \sum_{i=1}^N x_i^h \ln(x_i^h) + \frac{Y}{X+Y} \sum_{i=1}^N x_i^k \ln(x_i^k) \right\} \quad (5)$$

where R is the ideal gas constant, N is the element species in the individual sublattice, and x_i^h and x_i^k are the mole fractions of the i th element in the sublattice h and k , respectively. In HHC-1, the values of X of carbon sublattice (h) and Y of metal sublattice (k) are equal to 1, and the value of $\sum_{i=1}^N x_i^h \ln(x_i^h)$ of carbon sublattice is equal to 0. Therefore, the mixing entropy of HHC-1 can be expressed as:

$$\Delta S_{\text{mix}} = -R/2 \sum_{i=1}^N x_i^k \ln(x_i^k) \quad (6)$$

From Equation 6, the ΔS_{mix} of HHC-1 per mole is calculated to be about 0.805R. By combining the calculated ΔH_{mix} of HHC-1 discussed above, the ΔG_{mix} is found to be negative using the Equation 3 ($\Delta G_{\text{mix}} = -2.863$ kJ·mol⁻¹) at room temperature (298 K), suggesting that the structure of HHC-1 is thermodynamically stable. To further explore the stability of HHC-1, we investigated the atomic displacements of different elements from the initial FCC lattice configuration upon relaxation based on the first-principles calculations. Figure 1C displays the magnitude of the displacement of each atom from its original position in the 100 independent starting supercells. Clearly, the atomic displacements from the FCC lattice are quite small in general, within the 2.5% of the lattice constants, which confirms the stability of HHC-1.

Encouraged by the theoretical calculations, we conducted above-mentioned experiment to fabricate HHC-1. XRD characterization was first conducted to analyze the phase composition of HHC-1. Figure 2A displays XRD patterns of the phase evolution for the mixture of the initial powders and HHC-1 during HP sintering process. Before the HP sintering process, the mixture of the initial powders

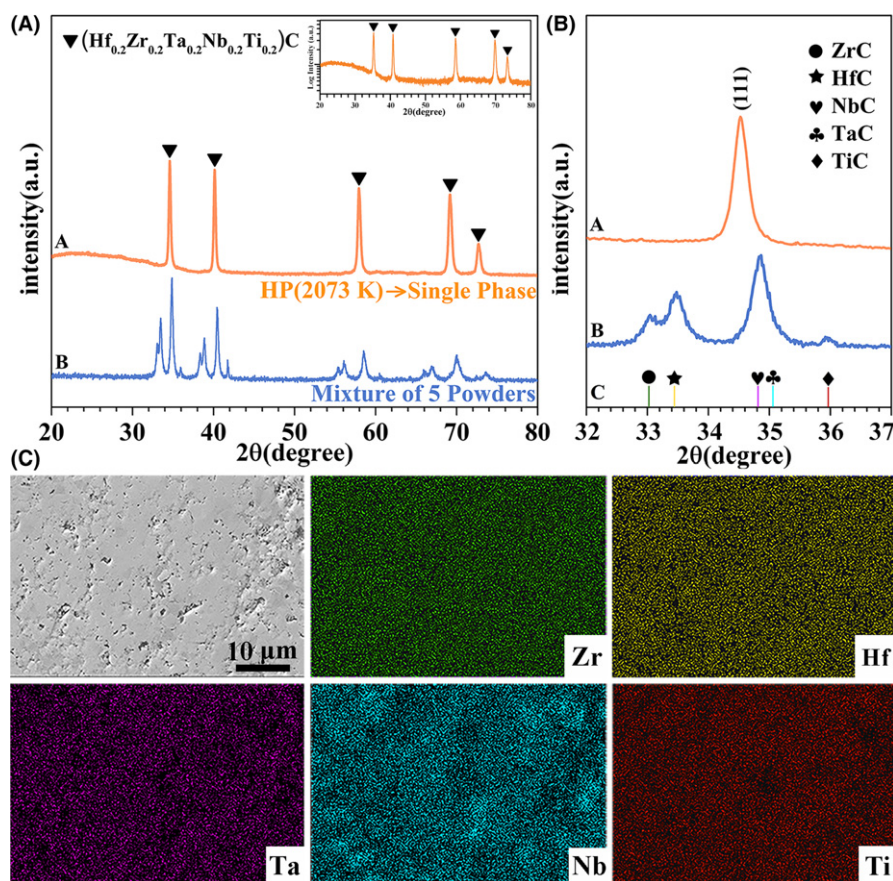


FIGURE 2 XRD and SEM characterizations of the different samples: (A) XRD patterns: A is HHC-1 and B is the mixture of five metal carbide powders; (B) enlargement of (A): C is the standard diffraction peaks from (111) planes of five metal carbides; (C) polished surface SEM image and the corresponding EDS compositional maps of HHC-1 [Color figure can be viewed at wileyonlinelibrary.com]

presents XRD diffraction peaks for five individual phases of the metal carbides. After the HP sintering process, those five individual metal carbide phases merged to form a single rock-salt crystal structure of metal carbides without other phases, as shown in Figure 2B, implying that HHC-1 is composed of the single rock-salt crystal structure of metal carbides. To further confirm this result, the X-ray data of HHC-1 in Figure 2A is plotted on a logarithmic scale, as shown in top-right corner in Figure 2A. Obviously, no any diffraction peaks of other phases can be found except for HHC-1, such as the individual binary carbides, oxides and other solid solutions. In addition, the lattice parameter of HHC-1 phase was measured to be about 4.497 Å by XRD, which is in good agreement with the lattice parameter from first-principles calculations (4.528 ± 0.005 Å). On the basis of this result, the theoretical density of HHC-1 can be calculated to be about 9.519 g/cm^3 . In HHC-1, the rearrangement of metallic elements will generate distinction in lattice parameters, which transfers the sublattice into an unstandardized rock-salt structure. That is to say, the lattice parameter and theoretical density are just the average estimation. Meanwhile, the measured density of HHC-1 using the Archimedes method is about 9.075 g/cm^3 . Therefore, the relative density of HHC-1 can be calculated to be about 95.3%. Figure 2C displays a typical SEM image of the polished surface and the corresponding EDS compositional maps of HHC-1. The compositions of HHC-1 are largely uniform at the micrometer scale except for the presence of a small quantity of Nb element localization. According to XRD results, the Nb element localization may be the undissolved NbC rather than the niobium oxides. In addition, EDS compositional maps from TEM analysis shows that no element localization can be observed at nanoscale, which suggests that the undissolved NbC exists in the microstructure as grain-boundary phase. The presence of a small quantity of undissolved NbC may result from the difference with other metal carbides in their electronic structure and atom radius.³² Generally, however, NbC can form continuous solid solutions with other metal carbides. Therefore, the presence of a small quantity of undissolved NbC can be dissolved by heating for a prolonged time or at higher temperatures.⁹ Therefore, the micrometer-scale compositional homogeneities of HHC-1 are largely satisfactory.

TEM analyses were employed to further investigate the crystal structure and compositional homogeneity at nanoscale. Figure 3A is a representative high-resolution transmission electron microscopy (HRTEM) image of HHC-1. It clearly exhibits a periodic lattice structure, in which a set of fringes is about 0.26 nm, corresponding to the d -space of (111) planes of FCC metal carbides. Moreover, the lattice parameter can be calculated to be about 4.468 Å, close to XRD results (4.496 Å). Selected area electron-

diffraction (SAED) pattern along the $[1 \bar{1} 0]$ zone axis (Figure 3B) indicates that HHC-1 is the typical FCC metal carbide structure, which is in good agreement with XRD results. Figure 3C presents the typical scanning transmission electron microscopy (STEM) image and EDS compositional maps at the nanometer scale. It can be observed that Zr, Hf, Ta, Nb, and Ti elements are uniformly distributed at nanoscale, and no segregation or aggregation is found throughout the scanned area. Combined to the results from XRD and SEM, it can be concluded that a single-phase HHC-1 with good compositional uniformity from nanoscale to microscale can be prepared by HP sintering technique, which verifies the rationalization of the first-principles calculations on analyzing the formation possibility of the high-entropy metal carbide ceramics.

The electrical resistivity and mechanical properties of HHC-1 were measured, as listed in Table 2 and compared with those of the individual binary carbides including ZrC, HfC, TaC, NbC, and TiC. Obviously, the measured electrical resistivity of HHC-1 is significantly higher than that of most of individual binary carbides, such as ZrC, HfC, NbC, and TaC, but is only comparable to that of TiC. The relatively high electrical resistivity is mainly due to the presence of solid solution effects and the porosity. The presence of solid solution effects is expected to improve the electrical resistivity associated to the following two aspects. In the one aspect, in HHC-1, the metal cations are in a disorder, that is, randomly occupy the cation sublattice, which will result in a high concentration of lattice distortion due to the different sizes and bonding strengths of five metal atoms (Hf, Zr, Ta, Nb, and Ti) in the cation position.¹² In the other aspect, the random carbon vacancies may be generated in HHC-1.³³ As a result, these lattice distortions and carbon vacancies can improve the scattering of the electron, which ultimately contributes to the relatively high electrical resistivity.³⁴ In addition, the relative density of ZHC-1 is only 95.1%, which indicates the presence of a certain amount of porosity in ZHC-1, the presence of the porosity in HHC-1 can also lead to an increase in electrical resistance because it can increase the scattering of the electron. For the mechanical properties of HHC-1, it is worth noticing that the nanohardness of HHC-1 is about $40.6 \pm 0.6 \text{ GPa}$ and its elastic modulus are in the range of 514 ± 10 – $522 \pm 10 \text{ GPa}$, which inherits the high nanohardness and elastic modulus of the binary carbides and even presents much higher values in nanohardness and elastic modulus than that of the individual binary carbides (Table 2) measured using identical nanoindentation techniques at approximately the same load. Furthermore, in order to avoid the effect of the estimated Poisson's ratio on the improvement of the elastic modulus, the reduced modulus was also listed in Table 2. Obviously, the reduced modulus of HHC-1 is much larger than that of the individual

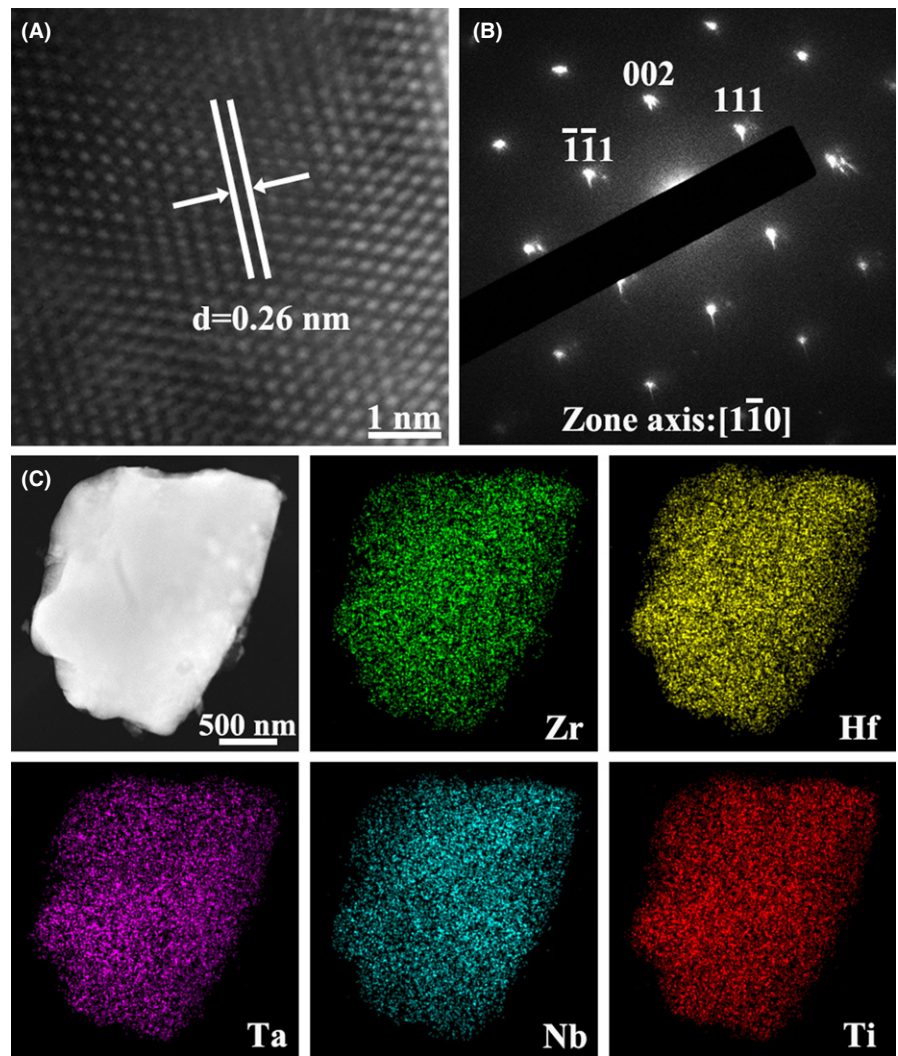


FIGURE 3 TEM analysis of HHC-1: (A) HRTEM image; (B) SAED pattern; (C) STEM image and the corresponding EDS compositional maps [Color figure can be viewed at wileyonlinelibrary.com]

TABLE 2 The measured electrical resistivity, nanohardness, elastic modulus, and reduced modulus of HHC-1 and five individual metal carbides using identical techniques

Samples	Electrical resistivity [$\mu\Omega\cdot\text{cm}$]	Nanohardness [GPa]	Elastic modulus [GPa]	Reduced modulus [GPa]	Load [mN]	References
ZrC	75	32.5	464	340	10	[36-38]
HfC	67	29.0	352	276	8	[36,39]
TaC	15	18.6	409	312	25	[36,40]
NbC	20	24.5	406	311	10	[36,41]
TiC	100	25.6	397	302	13	[36,42]
HHC-1	91 ± 1.3	40.6 ± 0.6	514 ± 10 – 522 ± 10	366	8	Present work

binary carbides, indicating that the elastic modulus has been improved. In view of the presence of the porosity in ZHC-1, the microhardness of HHC-1 was measured under different loads and the results are shown in Figure 4. It can be seen that the microhardness of HHC-1 exhibits a decrease trend with the increase in the load. Clearly, the microhardness of HHC-1 is about 22.5 ± 0.3 GPa at a load

of 0.98 N. While the microhardness of HHC-1 decreases to 18.8 ± 0.4 GPa when the load increases to 9.8 N, which is close to the value reported by Yan et al.¹² In addition, the measured microhardness of HHC-1 is much lower than that of the measured nanohardness. The decrease in the microhardness can be attributed to the presence of the porosity in HHC-1. In sum, however, the nanohardness and elastic

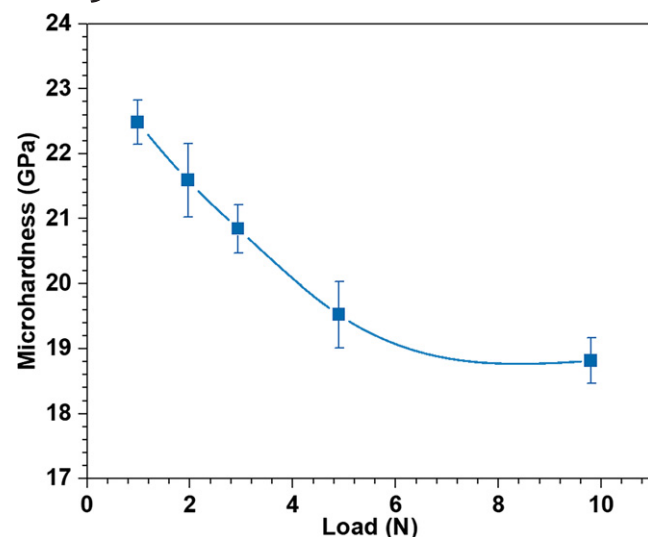


FIGURE 4 The measured microhardness of HHC-1 as a function of the load [Color figure can be viewed at [wileyonlinelibrary.com](https://onlinelibrary.wiley.com)]

TABLE 3 Comparison of the fracture toughness (K_{IC}) of HHC-1 with five individual metal carbides

Samples	Fracture toughness (K_{IC} , MPa/m ^{1/2})	Load (N)	Equation	References
ZrC	2.1 ± 0.2	19.6	Anstis	[37]
HfC	2.9 ± 0.5	9.8	Anstis	[43]
TaC	2.7 ± 0.3	9.8	Anstis	[43]
NbC	2.9 ± 0.2	98	Lawn	[44]
TiC	3.3 ± 0.1	9.8	Anstis	[45]
HHC-1	3.0 ± 0.2	24.5	Anstis	Present work

modulus of HHC-1 is much larger compared with that of the individual binary carbides, which is due to the presence of solid solution strengthening mechanism. During the HHC-1 solid solution formation, the distortion can be introduced into the lattices at a specific degree. Nevertheless, from the thermal dynamical point of view, the entire crystal lattices potentially maintain the original lattice configurations, and therefore the local stress fields will be created. The presence of the stress fields further result in an increase in hardness.⁴ In general, most inorganic materials possess a positive correlation between elastic modulus and interatomic bonding.³⁵ For solid solutions, the smaller mixing enthalpy means the larger binding force between elements.^{4,29} On the basis of the first-principles calculations, the value of the mixing enthalpy is negative. This indicates that the interatomic bonding of HHC-1 is rather strong, leading to the increase in elastic modulus. Therefore, the as-observed enhancement in hardness and elastic modulus of HHC-1 should be relevant to the presence of solid solution strengthening mechanism in high-entropy ceramics.

Nevertheless, the fracture toughness of HHC-1 is close to the value of the individual binary carbide (Table 3). This indicates that the impact of solid solution effects on the toughness of high-entropy ceramics can be negligible.

4 | CONCLUSION

In conclusion, we had theoretically demonstrated the formation possibility of HHC-1 based on the first-principles calculations and then successfully fabricated a single-phase HHC-1 by HP sintering technique. The HHC-1 not only had a near zero mixing enthalpy but also possessed a high mixing entropy, which made the structure of HHC-1 be thermodynamically stable. The as-prepared HHC-1 exhibited a single rock-salt crystal structure of metal carbides and the high compositional uniformity from nanoscale to microscale. Therefore, it had extremely high nanohardness and elastic modulus and relatively high electrical resistivity, which could be attributed to the presence of solid solution effects. These superior performances endow the high-entropy metal carbide ceramics a promising candidate for extreme environmental applications.

ACKNOWLEDGMENTS

B. Ye, K. Huang, and Y. Chu acknowledge the financial support from the National Key Research and Development Program of China (No. 2017YFB0703200), National Natural Science Foundation of China (No. 51802100), and Young Elite Scientists Sponsorship Program by CAST (No. 2017QNRC001). Work at Ames Laboratory was supported by the U.S. Department of Energy, Basic Energy Sciences, Division of Materials Science and Engineering. Ames Laboratory is operated for the U.S. DOE by Iowa State University under Contract No. DE-AC02-07CH11358. The computer time support came from National Energy Research Scientific Computing Center (NERSC) in Berkeley, CA.

CONFLICT OF INTEREST

The authors declare no competing financial interest.

AUTHOR CONTRIBUTIONS

Y. Chu conceived and designed the experiments. Y. Chu, B. Ye, and K. Huang performed the experiments. Y. Chu and B. Ye analyzed the data. T. Wen and C.-Z. Wang performed the first-principles calculations. All authors commented on the manuscript.

ORCID

Yanhui Chu  <https://orcid.org/0000-0001-6158-7501>

REFERENCES

- Rost CM, Sachet E, Borman T, Moballegh A, Dickey EC, Hou D, et al. Entropy-stabilized oxides. *Nat Commun*. 2015;6:8485.
- Jiang S, Hu T, Gild J, Zhou N, Nie J, Qin M, et al. A new class of high-entropy perovskite oxides. *Scripta Mater*. 2018;142:116–20.
- Zhang Y, Zuo TT, Tang Z, Gao MC, Dahmen KA, Liaw PK, et al. Microstructures and properties of high-entropy alloys. *Prog Mater Sci*. 2014;61:1–93.
- Miracle DB, Senkov ON. Critical review of high entropy alloys and related concepts. *Acta Mater*. 2017;122:448–511.
- Tsai MH, Yeh JW. High-entropy alloys: a critical review. *Mater Res Lett*. 2014;2:107–23.
- Yeh JW, Chen SK, Lin SJ, Gan JY, Chin TS, Shun TT, et al. Nanostructured high-entropy alloys with multiple principal elements: novel alloy design concepts and outcomes. *Adv Eng Mater*. 2004;6:299–303.
- Anand G, Wynn AP, Handley CM, Freeman CL. Phase stability and distortion in high-entropy oxides. *Acta Mater*. 2018;146:119–25.
- Gild J, Samiee M, Braun JL, Harrington T, Vega H, Hopkins PE, et al. High-entropy fluorite oxides. *J Eur Ceram Soc*. 2018;38:3578–84.
- Gild J, Zhao Y, Harrington T, Jiang S, Hu T, Quinn MC, et al. High-entropy metal diborides: a new class of high-entropy materials and a new type of ultrahigh temperature ceramics. *Sci Rep*. 2016;6:37946.
- Mayrhofer PH, Kimbauer A, Ertelthaler Ph, Koller CM. High-entropy ceramic thin films; A case study on transition metal diborides. *Scripta Mater*. 2018;149:93–7.
- Jin T, Sang X, Unocic RR, Kinch RT, Liu X, Hu J, et al. Mechanochemical-Assisted synthesis of high-entropy metal nitride via a soft urea strategy. *Adv Mater*. 2018;30:1707512.
- Yan X, Constantin L, Lu Y, Silvain J, Nastasi M, Cui B. $(\text{Hf}_{0.2}\text{Zr}_{0.2}\text{Ta}_{0.2}\text{Nb}_{0.2}\text{Ti}_{0.2})\text{C}$ high-entropy ceramics with low thermal conductivity. *J Am Ceram Soc*. 2018;101:4486–91.
- Zhou J, Zhang J, Zhang F, Niu B, Lei L, Wang W. High-entropy carbide: a novel class of multicomponent ceramics. *Ceram Int*. 2018;44:22014–8.
- Häglund J, Guillermet AF, Grimvall G, Körling M. Theory of bonding in transition-metal carbides and nitrides. *Phys Rev B*. 1993;48:11685.
- Oyama ST. *The chemistry of transition metal carbides and nitrides*. Scotland: Blackie Academic and Professional; 1996.
- Kresse G, Furthmüller J. Efficient iterative schemes for ab initio total-energy calculations using a plane-wave basis set. *Phys Rev B*. 1996;54:11169.
- Kresse G, Hafner J. Ab initio molecular dynamics for liquid metals. *Phys Rev B*. 1992;47:558.
- Weingarten NS, Byrd EF. Special quasirandom structures of alon. *Comput Mater Sci*. 2015;96:312–8.
- Perdew JP, Burke K, Ernzerhof M. Generalized gradient approximation made simple. *Phys Rev Lett*. 1996;77:3865–8.
- Yalamanchili K, Wang F, Schramm IC, Andersson JM, Joesaar MPJ, Tasnadi F, et al. Exploring the high entropy alloy concept in $(\text{AlTiVNbCr})\text{N}$. *Thin Solid Films*. 2017;636:346–52.
- Ha D, Kim J, Han J, Kang S. Synthesis and properties of $(\text{Hf}_{1-x}\text{Ta}_x)\text{C}$ solid solution carbides. *Ceram Int*. 2018;44:19247–53.
- Urban A, Abdellahi A, Dacek S, Artrith N, Ceder G. Electronic-structure origin of cation disorder in transition-metal oxides. *Phys Rev Lett*. 2017;119:176402.
- Monkhorst HJ, Pack JD. Special points for Brillouin-zone integrations. *Phys Rev B*. 1977;16:1748–9.
- Oliver WC, Pharr GM. An improved technique for determining hardness and elastic-modulus using load and displacement sensing indentation experiments. *J Mater Res*. 1992;7:1564–83.
- Lu XG, Selleby M, Sundman B. Calculations of thermophysical properties of cubic carbides and nitrides using the Debye-Grüneisen model. *Acta Mater*. 2007;55:1215–26.
- Anstis GR, Chantikul P, Lawn BR, Marshall DB. A critical evaluation of indentation techniques for measuring fracture toughness: Indirect crack measurements. *J Am Ceram Soc*. 1981;64:533–8.
- Vegard L. Die konstitution der mischkristalle und die raumfüllung der atome. *Z Phys*. 1921;5:17–26.
- Shulumba N, Hellman O, Raza Z, Alling B, Barrirero J. Lattice vibrations change the solid solubility of an alloy at high temperatures. *Phys Rev Lett*. 2016;117:205502.
- Yang X, Zhang Y. Prediction of high-entropy stabilized solid-solution in multi-component alloys. *Mater Chem Phys*. 2012;132:233–8.
- Andersson JO, Guillermet AF, Hillert M, Jansson B, Sundman B. A compound-energy model of ordering in a phase with sites of different coordination numbers. *Acta Metall*. 1986;34:437–45.
- Dematteis EM, Santoru A, Poletti MG, Pistidda C, Klassen T, Dornheim M, et al. Phase stability and hydrogen desorption in a quinary equimolar mixture of light-metals borohydrides. *Int J Hydrogen Energ*. 2018;43:16793–803.
- Dai FZ, Zhou Y, Sun W. Segregation of solute atoms (Y, Nb, Ta, Mo and W) in ZrB_2 grain boundaries and their effects on grain boundary strengths: a first-principles investigation. *Acta Mater*. 2017;127:312–8.
- Williams WS. Electrical properties of hard materials. *Int J Refract Met Hard Mater*. 1999;17:21–6.
- Zhang Y, Stocks GM, Jin K, Lu C, Bei H, Sales BC, et al. Influence of chemical disorder on energy dissipation and defect evolution in concentrated solid solution alloys. *Nat Commun*. 2015;6:8736.
- Pierson HO. *Handbook of refractory carbides and nitrides: properties, characteristics, processing and applications*. New Jersey: Noyes Publications; 1996.
- Riedel R. *Handbook of ceramic hard materials*. Germany: Wiley-VCH; 2008.
- Sciti D, Guicciardi S, Nygren M. Spark plasma sintering and mechanical behaviour of ZrC-based composites. *Scripta Mater*. 2008;59:638–41.
- Balko J, Csanadi T, Sedlak R, Vojtko M, Kovalikova A, Koval K, et al. Nanoindentation and tribology of VC, NbC and ZrC refractory carbides. *J Eur Ceram Soc*. 2017;37:4371–7.
- Kurbatkina VV, Patsera EI, Levashov EA, Timofeev AN. Self-propagating high-temperature synthesis of single-phase binary tantalum-hafnium carbide (Ta, Hf) C and its consolidation by hot pressing and spark plasma sintering. *Ceram Int*. 2018;44:4320–9.
- Shao TT, Cai X, Wang J, Zhong L, Zhao N, Xu Y. Research on mechanical characteristic of micro-nano structure TaC ceramic by nanoindentation. *Adv Mater Res*. 2015;1120:11–5.
- Wu L, Wang Y, Yan Z, Zhang J, Xiao F, Liao B. The phase stability and mechanical properties of Nb-C system: using first-

- principles calculations and nano-indentation. *J Alloys Comp.* 2013;561:220–7.
42. Teber A, Schoenstein F, Tetard F, Abdellaoui M, Jouini N. The effect of Ti substitution by Zr on the microstructure and mechanical properties of the cermet $Ti_{1-x}Zr_xC$ sintered by SPS. *Int J Refract Met Hard Mater.* 2012;31:132–7.
 43. Cedillos-Barraza O, Grasso S, Nasiri NA, Jayaseelan DD, Reece MJ, Lee WE. Sintering behaviour, solid solution formation and characterisation of TaC, HfC and TaC-HfC fabricated by spark plasma sintering. *J Eur Ceram Soc.* 2016;36:1539–48.
 44. Demirskyi D, Sakka Y, Vasylykiv O. High-temperature reactive spark plasma consolidation of TiB_2 -NbC ceramic composites. *Ceram Int.* 2015;41:10828–34.
 45. Acicbe RB, Goller G. Densification behavior and mechanical properties of spark plasma-sintered ZrC-TiC and ZrC-TiC-CNT composites. *J Mater Sci.* 2013;48:2388–93.

How to cite this article: Ye B, Wen T, Huang K, Wang C-Z, Chu Y. First-principles study, fabrication, and characterization of $(Hf_{0.2}Zr_{0.2}Ta_{0.2}Nb_{0.2}Ti_{0.2})C$ high-entropy ceramic. *J Am Ceram Soc.* 2019;102: 4344–4352. <https://doi.org/10.1111/jace.16295>